# Water vapor transport properties of interfacially polymerized thin film nanocomposite membranes modified with graphene oxide and GO-TiO$_2$ nanofillers

Muhammad Irshad Baig[a,b], Pravin G. Ingole[c,*], Jae-deok Jeon[a], Seong Uk Hong[d], Won Kil Choi[a], Hyung Keun Lee[a,*]

[a] Korea Institute of Energy Research (KIER), 71-2 Jang-dong, Yuseong-gu, Daejeon 34129, Republic of Korea
[b] Membrane Science and Technology, MESA + Institute for Nanotechnology, University of Twente, Faculty of Science and Technology, P.O. Box 217, 7500 AE Enschede, The Netherlands
[c] Chemical Engineering Group, Engineering Sciences and Technology Division, CSIR-North East Institute of Science and Technology, Jorhat 785006, Assam, India
[d] Department of Chemical and Biological Engineering, Hanbat National University, 125 Dongseodaero, Yuseong-gu, Daejeon 34158, Republic of Korea

## HIGHLIGHTS

- GO and GO-TiO$_2$ nanofillers were incorporated in polyamide nanocomposite membrane.
- Improved water vapor permeance was obtained from GO and GO-TiO$_2$ nanofillers incorporated TFN membranes.
- Highly hydrophilic TFN membranes were obtained for water vapor separation.
- GO-TiO$_2$ shows superior water vapor permeance than GO.
- Functionalized GO could improve water vapor permeation even further.

## GRAPHICAL ABSTRACT

GO and GO-TiO$_2$ incorporation in TFN membrane by interfacial polymerization for excellent water vapor separation performance.
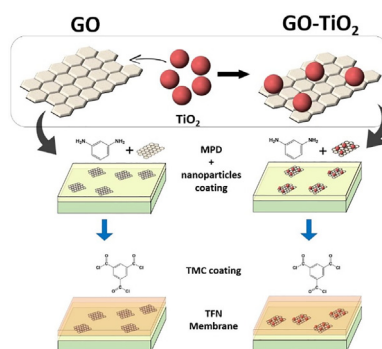


## ARTICLE INFO

## ABSTRACT

Graphene oxide (GO) and its composite with TiO$_2$ (GT) were utilized as nano-filler materials to prepare highly permeable and water vapor selective nanocomposite membranes. The nano-fillers were characterized using different analytical tools to determine their physicochemical properties. Nanocomposite membranes were prepared by dispersing the nano-fillers in aqueous phase monomer solution for interfacial polymerization reaction on the inner surface of Polysulfone hollow fiber membrane. Surface morphology and bonding chemistry of the nanocomposite membrane was analyzed using various analytical tools. The two types of nano-fillers were compared for their compatibility with the polyamide matrix, and consequently, the water vapor separation performance of the resulting membrane. Results revealed that both the nano-fillers are firmly attached to the polyamide layer via hydrogen and covalent bonds. GT based membranes have higher surface roughness and better hydrophilicity as compared to GO. In addition, GT membranes have more carboxyl groups and lesser degree of cross-linking due to the interference with interfacial polymerization reaction. This leads to a higher permeance (2820 GPU) and a water vapor/nitrogen selectivity when compared to other TFN membranes

* Corresponding authors.
  E-mail addresses: ingolepravin@gmail.com (P.G. Ingole), hklee@kier.re.kr (H.K. Lee).

reported in literature. The nano-fillers act as active sites for preferential transport of water vapor molecules through the membrane thereby, significantly improving water vapor permeance.

## 1. Introduction

Water vapor is a dominant greenhouse gas. In clear skies, the contribution of water vapor to the greenhouse effect is approximately 60%, followed by carbon dioxide ($\sim 25\%$), ozone ($\sim 8\%$) and other trace gases [1]. With the amount of carbon dioxide that exists in the earth's atmosphere, increasing water vapor content (relative humidity) amplifies the heat trapping effect of $CO_2$, thus resulting in a potent impact on global warming. An enormous amount of water vapor is released into the atmosphere by a number of industries including power plants and chemical factories. This gradual moistening of the earth's troposphere has increased the global warming effect of $CO_2$ by two folds [2]. With the increased use of greener technologies to curb $CO_2$ emissions, there is also a greater need to address the water vapor emissions from man-made sources. In addition to large industrial units such as cooling towers, removal of water vapor is also crucial in applications such as dehumidification and air conditioning of buildings [3].

Currently, water vapor is removed from industrial cooling towers and air dehumidification units by a number of techniques such as desiccant drying [4], gas condensation [5], and membrane technology [6]. Among these, the polymeric membrane technology has been commercially implemented since the 1970's due to its smaller footprint and relatively simple operation [6]. Separation is achieved using membranes that have a dense top layer and a porous support. Thin film composite (TFC) and nanocomposite (TFN) membranes meet these requirements. These composite membranes are mostly prepared through an interfacial polymerization (IP) reaction of two or more monomers on the surface of a porous polymeric support. Research on TFC membranes for gas separation surged after Cadotte et al. [7] proposed interfacial polymerization (IP) as a feasible method to prepare a selective polyamide layer [7]. The polyamide layer possesses desirable characteristics such as mechanical strength, chemical resistance, and thermal stability coupled with high selectivity which is essential in gas separation [8]. The major aim in gas separation membranes is to overcome the upper limit of permeance-selectivity trade-off curve, commonly known as the 'Robeson Plot'. With the optimum reaction conditions already known for TFC membranes, [9–11] it is becoming increasingly difficult to overcome this upper bound.

A new path towards developing the next generation of composite membranes was introduced when Jeong et al. successfully demonstrated that adding Zeolite A nanoparticles in the polyamide matrix during the IP reaction can give highly permselective thin film nanocomposite membranes for reverse osmosis application [12]. Nanoparticles inclusion in the polyamide layer makes it much easier to control its properties because of the high surface area and surface energy of nanoparticles [13]. Highly permeable and selective gas separation membranes can be produced by simply tuning the type of nanoparticles, their size, and surface chemical properties.

Wide variety of nanomaterials have been used as nano-fillers for gas separation membranes. A filler material shall ideally have a small size ($< 100\,nm$) because most polyamide layers are of hundred nanometers thick. Furthermore, it should also be compatible with the polyamide matrix by forming covalent bonds. Recently, Gao et al. synthesized polyethyleneimine grafted ZIF-8 particles for $CO_2$ separation [14]. The modified porous ZIF-8 particles were found to have better compatibility with the polymer matrix while maintaining high permselectivity. Shamsabadi et al. proposed $TiO_2$ nanoparticles as nano-fillers for $CO_2/N_2$ separation membranes [15]. Similarly, other nanomaterials such as carbon nanofibers and nanotubes [16,17], silica [18], and metal organic frameworks [19,20] have been used as filler materials for gas

separation membranes because of their tunable properties and pore structures. Recently, researchers have shown that incorporating graphene oxide in the polyamide layer for $CO_2$ separation results in an acceptable permeance and selectivity trade-off [21,22]. Apart from above mentioned applications, membranes are widely used in solar cells and batteries [23,24]. Applying phase inversion method Li et al. prepared porous membranes using polyetherimide with tunable morphology and for lithium-ion batteries (LIBs) [25]. Recently researchers have also developed different eggshell membranes for lithium-ion battery along with membranes for vanadium redox flow battery applications [26,27].

However, the use of nanoparticles in TFN membranes is mainly limited to conventional gas separation applications such as $CO_2/N_2$, $CO_2/CH_4$ etc. In our previous work, we have demonstrated that functionalized silicon nanoparticles (15–20 nm) are resistant to agglomeration at low concentrations and exhibit high water vapor permeance and selectivity [28]. Similarly, in previous research, used $TiO_2$ nanoparticles and acid activated bentonite clay to fabricate highly hydrophilic nanocomposite membranes for improved water vapor permeance [29,30]. Use of new nanomaterials for gas separation applications is essential in order to overcome the trade-off between permeance and selectivity.

In this work, we have improved the water vapor permeance and selectivity of TFN membranes by utilizing two types of nano-fillers. We have incorporated graphene oxide (GO) and Graphene oxide-$TiO_2$ (GT) as a filler material in the polyamide selective layer. GO has gained wide spread attention because of its abundant hydroxyl and carboxyl groups that form hydrogen networks with water molecules [31]. Furthermore, graphene oxide has a better dispersion in water and polar solvents which makes it easier to be used in IP reaction [32]. GO based TFN membranes have already been shown to increase the water permeability for nanofiltration applications [33–35]. In addition, when coupled with $TiO_2$ nanoparticles, GO-$TiO_2$ composites have further increased the membrane separation performance [36]. The synergistic effects of using two nanomaterials at once can lead to an improved water vapor separation. Herein, we examine how GO and GO-$TiO_2$ affects the polyamide layer and its bonding chemistry. The aim is to increase the water vapor permeance and selectivity while adding only minimum amount of nano-fillers. It is hoped that the findings of this research will contribute to a deeper understanding of the nanomaterials and their interaction with water vapor.

## 2. Experimental

### 2.1. Materials

Polysulfone ultrafiltration hollow fiber membranes, having an outer diameter of 1400 μm and inner diameter of 1000 μm, were obtained from Guiyang Shidai Huitong Film Technology Co. Ltd. China. The molecular weight cut-off of the purchased membranes was 8000 Da. Graphene oxide dispersion solution in $H_2O$ (2 mg/ml, GO), $TiO_2$ nanoparticles (average particle size $\sim 70\,nm$), $m$-Phenylenediamine (99%, MPD) and 1,3,5-Benzenetricarbonyl trichloride (98%, TMC) were purchased from Sigma-Aldrich. $n$-Hexane (95%), which was used as the solvent for TMC, was purchased from Duksan Pure Chemicals. Deionized water was obtained from a Millipore (Milli-Q) water purification system. All the chemicals were used as received. Pure Nitrogen gas (99.99%) for the inside coating system and the water vapor permeation test was purchased from Safety Gas Korea.

## 2.2. Preparation of GO-TiO$_2$ composite

As-received graphene oxide solution was sonicated for 1 h to fully exfoliate the GO sheets. Afterwards, the graphene oxide-TiO$_2$ composite was prepared by dispersing TiO$_2$ nanoparticles in GO solution. Weight of TiO$_2$ nanoparticles was carefully measured using an electronic weight balance before adding to the GO solution in 3:2 (GO:TiO$_2$) ratio. Excess GO suppresses the photocatalytic activity of TiO$_2$ and also helps in preventing its leaching out due to the increased interaction with GO nano-sheets. The mixture was stirred continuously for 24 h at ambient conditions followed by sonication for 2 h. The resulting mixture showed uniform dispersion, Fig. S1 (Supplementary information). It is well known that TiO$_2$ nanoparticles are well-dispersed and uniformly attached onto the surface of graphene oxide sheets under ultrasonic conditions [37]. This method gives increased interaction between the nanoparticles and GO sheets resulting in a higher surface area.

## 2.3. Preparation of nanocomposite polyamide (PA) layer

Five hollow fiber membranes were bundled together and inserted in a 30 cm long cylindrical module. Both ends of this 1 inch diameter module were sealed using a polyurethane epoxy. The excess epoxy on both sides was cut to expose the tube side of the fibers. Monomers for interfacial polymerization reaction were prepared by dissolving 2.0 wt % MPD in deionized water and 0.2 wt% TMC in *n*-Hexane. Two sets of nanocomposite membranes were prepared in this experiment: GO and GT based TFN membranes, where GT stands for GO-TiO$_2$. For the first set (GO based nanocomposite membranes), the sonicated graphene oxide dispersion solution was added to the aqueous phase monomer in various concentrations with respect to MPD. Similarly, for the second set (GT based nanocomposite membranes) GO-TiO$_2$ dispersion solution was added to MPD solution under constant stirring at room temperature. The MPD solution containing the nano-fillers was further sonicated for 1 h to ensure a uniform dispersion. All the membranes were washed with deionized water and subsequently dried using N$_2$ gas to remove any dirt or preservative chemicals. The cylindrical modules were then mounted on an inside coating machine to fabricate nano-composite layer on the inner surface of hollow fiber membranes. The coating conditions were kept the same for both sets of TFN membranes. MPD solution containing the nano-fillers was first fed from the tube side of the module for 10 mins followed by N$_2$ gas purging for 3 mins to remove the excess monomer. Next, the TMC solution was fed from the tube side for 5 mins and the excess monomer was dried by purging N$_2$ gas for 3 mins. Heat treatment of the membrane modules was performed at 70 °C for 10 mins in order to further strengthen the newly formed polyamide layer.

Graphene oxide based TFN membranes were named GO (conc.) and the GO-TiO$_2$ based TFN membranes were named as GT (conc.) where the concentration in weight % of the nano-fillers is mentioned in the parenthesis. The experimental parameters for the preparation of nanocomposite membranes is outlined in Table 1.

## 2.4. Physicochemical characterization of thin film nanocomposite membranes

Polyamide nanocomposite membranes were characterized using various analytical tools. The amide functionalities in the membrane were identified by attenuated total reflectance Fourier Transformed infrared spectroscopy (ATR-FTIR) performed on ALPHA-P Spectrometer (Bruker Optik GmbH) in the wavenumber range 600–4000 cm$^{-1}$. The inner surface of hollow fiber membrane was exposed such that the nanocomposite layer faced the ATR diamond crystal. GO and GO-TiO$_2$ nanoparticle composites were visualized using high-resolution transmission electron microscopy (HR-TEM) performed on JEM-2100F (HR) advanced Field Emission Electron Microscope. Nano-fillers were visualized by putting a droplet of respective solutions on a copper mesh

holder and letting the water evaporate under ambient conditions. Field emission scanning electron microscopy (FE-SEM) was performed on Nova NanoSEM 450 (FEI, USA) equipped with energy dispersive X-ray spectroscopy (EDX) Quantax 200, Bruker. Cross-section morphology of the nanocomposite hollow fiber membranes was visualized by freezing the internal structure of fibers in liquid nitrogen before placing them on the sample holder. Before taking FE-SEM images, all the samples were sputter coated with a thin layer of gold using SCD 040 (Balzers Union, Liechtenstein). Atomic force microscopy (AFM) was performed on XE–100 (Park Systems, South Korea) to analyze the surface roughness profiles of the nanocomposite membranes. The data was obtained in terms of average surface roughness (R$_a$), maximum surface roughness (R$_{max}$), root mean square surface roughness (R$_q$), and geometric surface area. Surface hydrophilicity was analyzed by sessile-drop technique using Phoenix 300 Plus (SEO Co. Ltd.) water contact angle analyzer which used deionized water as the probe liquid. Hollow fiber membranes were cut open and the nanocomposite polyamide layer was exposed to the micro-syringe of the analyzer. A deionized water droplet of 3 µL was dispensed electronically from the micro-syringe. Contact angle of the droplet was measured at five different locations for two different membranes and the average of left and right angle was taken. All the measurements were taken 15 s after the droplet touched the surface. Measurements were conducted in a controlled environment to negate the effects of temperature and humidity. However, the contact angle alone is not sufficient to accurately quantify the hydrophilicity of the membranes because of the varying surface morphology, porosity and capillary effects [10]. Therefore, the surface hydrophilicity was quantified using solid-liquid interfacial free energy ($-\Delta G_{SL}$) that increases as a function of hydrophilicity. Modified Young-Dupre equation, Eq. (1), calculates the interfacial free energy of a surface using the average water contact angle (θ) in degrees, surface tension of water (γ$_L$, 72.8 $mJ/m^2$) and relative surface area (Δ) [38]. Relative surface area is the ratio of the actual surface area obtained by AFM, to that of the area of a smooth surface of the same dimensions.

$$-\Delta G_{SL} = \gamma_L \left[ 1 + \frac{\cos\theta}{\Delta} \right] \tag{1}$$

Surface chemical composition of the TFN membranes was analyzed using X-ray photoelectron spectroscopy (XPS) on MultiLab 2000 spectrometer (Thermo Electron Corporation, England). Monochromatic Aluminum $K_\alpha$ radiation was used as the X-ray source with a characteristic energy of 1485.6 eV, running at 150 W with constant analyzer pass energy of 160 eV. High resolution XPS scan was conducted for C, N, and O atoms with a resolution of 0.1 eV. Calibration for the binding energy was done using Carbon (1s) 285 eV as a reference standard. Thermal stability of the nanocomposite membranes was characterized by thermal gravimetric analysis (TGA) performed on a SDT Q600 (TA Instruments, USA). The samples were heated from room temperature to 800 °C in a N$_2$ atmosphere at the heating rate of 10 °C/min. For all the analysis techniques, a minimum of three membrane samples were taken to achieve reproducible results.

## 2.5. Water vapor mixed gas permeation experiments

The water vapor permeation tests were conducted on the setup

**Table 1**
Experimental conditions for interfacial polymerization reaction.

| Membrane name | GO/GT concentration (wt%) with respect to MPD |
|---|---|
| GO or GT (0.05) | 0.05 |
| GO or GT (0.1) | 0.1 |
| GO or GT (0.2) | 0.2 |
| GO or GT (0.5) | 0.5 |
| GO or GT (1.0) | 1.0 |
| GO or GT (2.0) | 2.0 |

which is described in detail in our previous work [39]. A schematic diagram of the mixed vapor/gas permeation setup is also shown in Fig. S2 (Supplementary information). Briefly, water vapor and nitrogen gas were mixed according to the desired humidity level and fed to the membrane module through the shell side. The feed pressure was maintained at 3.0 kg-f/cm$^2$ using a back pressure regulator. The relative humidity of feed gas was increased by increasing the flow rate of the carrier gas (water vapor/N$_2$ mixture) at the expense of dilution gas (pure N$_2$) while keeping the feed flow rate constant at 1000 cm$^3$/min. Relative humidity and gas temperature was measured at feed and retentate sides using humidity and temperature transmitter (HMT), Probe type 344 Vaisala Oyj, Finland. The pressure at permeate stream was maintained at 0.2 kg-f/cm$^2$ using a vacuum pump. Flow rate at the permeate stream was measured after it passed through a cold trap (CTB-10 JEIO Tech., Korea) using a bubble flow meter (Gillibrator, USA). All the permeation experiments were carried out at 30 °C by keeping the membrane module in a temperature controlled oven and preheating the gas before it enters the module. All the measurements were taken once the system reached a steady state.

Water vapor permeance and selectivity were calculated using a procedure described in detail elsewhere [40]. Briefly, the flow rate at permeate stream was converted into flux by dividing it with effective membrane area (40.8 cm$^2$). The resulting flux was converted to permeance by dividing it with partial pressure difference between feed and permeate sides. The permeance is reported in gas permeation unit, GPU, where 1 GPU = $1 \times 10^{-6}$ cm$^3$ (STP)/(cm$^2$.s.cmHg). The water vapor/N$_2$ selectivity was obtained by taking a ratio of water vapor permeance to N$_2$ permeance.

# 3. Results and discussion

## 3.1. Characteristics of the thin film nanocomposite membranes

### 3.1.1. ATR-FTIR

FTIR spectra of the pristine Polysulfone ultrafiltration membrane and the thin film nanocomposite membranes are presented in Fig. 1. Typical infrared spectra showing the characteristic peaks of Polysulfone (PSf) were obtained in accordance with the reported literature [41].
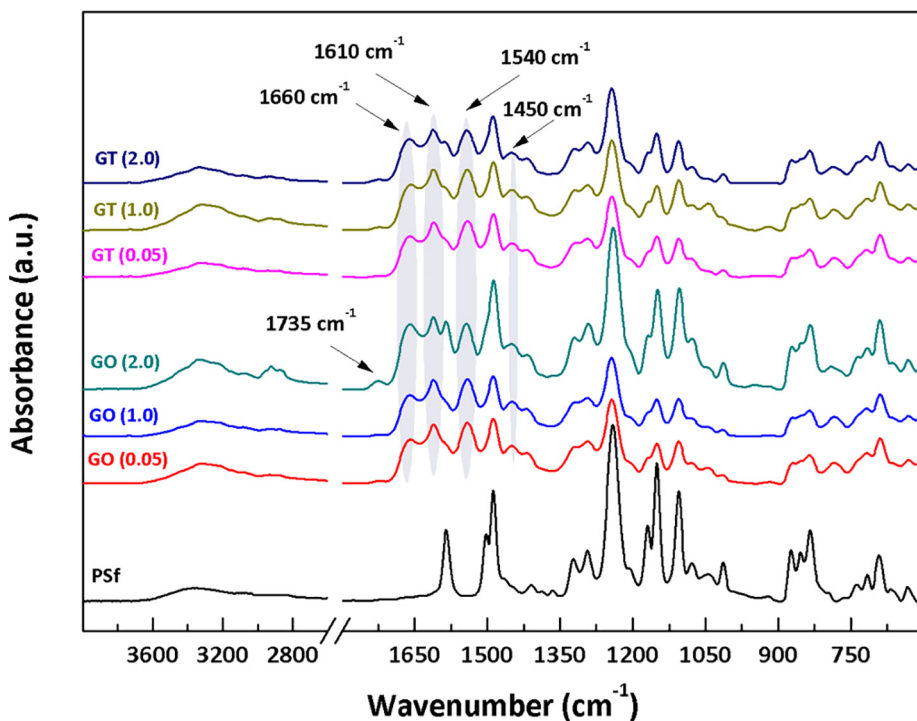
The peaks at 1580 cm$^{-1}$ and 1486 cm$^{-1}$ are assigned to the aromatic C−C stretching of the sulfone group, 1323 cm$^{-1}$ and 1293 cm$^{-1}$ are characteristic peaks of asymmetric SO$_2$ stretching vibration, the peak at 1250 cm$^{-1}$ can be assigned to the C−O−C stretching of the aryl ether group and the characteristic peak at 1150 cm$^{-1}$ is assigned to the symmetric O=S=O stretching of the sulfone group. Moreover, the peak ~ 830 cm$^{-1}$ is assigned to the in-phase-out-of-plane hydrogen deformation of *para*-substituted phenyl group [41].

The infrared spectra of GO was also collected and is shown in Fig. S3 (Supplementary information). The broad absorption band at ~ 3420 cm$^{-1}$ is assigned to the –OH groups, the peaks at ~ 1723 cm$^{-1}$ and ~ 1630 cm$^{-1}$ are attributed to C=O stretching vibration of carboxyl and carbonyl moieties functional groups. The two absorption peaks at ~ 1220 cm$^{-1}$ and ~ 1044 cm$^{-1}$ are characteristic C−O stretching vibrations [42].

The infrared spectra of the nanocomposite membranes incorporating GO and GO-TiO$_2$ are also shown in Fig. 1. The characteristic absorption peaks of polyamide appeared at 1660 cm$^{-1}$, 1610 cm$^{-1}$, and 1540 cm$^{-1}$, which are attributed to the C=O stretching vibrations (amide I), aromatic ring breathing (N−H stretching of the amide) N−H bending (amide II), and C−N stretch of the amide, respectively [43]. The absorption peak that is only present in nanocomposite membranes appears at 1450 cm$^{-1}$ and can be attributed to the carboxylic acid group (C=O stretching/O−H bending of carboxylic acid). This peculiar absorption band appears in nanocomposite membranes because the acid groups of TMC hydrolyze and form carboxyl acid groups. Interestingly, a weak absorption band at 1580 cm$^{-1}$ only appears in membranes GO (2.0) and GT (2.0). This band can be related to the C=C aromatic stretching which arises due to comparatively higher concentration of graphene oxide in the TFN membrane. The broad absorption band at around 3300 cm$^{-1}$ is attributed to the stretching of hydroxyl groups attached to the basal plane of GO. Another interesting absorbance peak appears at 1735 cm$^{-1}$ in GO (2.0) spectra. This band is associated with C=O stretch of ester. The formation of ester is due to the interaction of GO and carboxyl groups of TMC, as shown in Fig. 2 [44]. This is because of the interference in interfacial polymerization reaction. The functional groups on GO nanosheets react with the carbonyl group of TMC thus depleting the



**Fig. 1.** ATR-FTIR spectra of pristine Polysulfone membrane and nanocomposite membranes prepared by interfacial polymerization of MPD (containing GO/GT) and TMC. The existence of polyamide layer is confirmed by the presence of absorbance bands at 1660 cm$^{-1}$ (C=O), 1610 cm$^{-1}$ (N−H) and 1540 cm$^{-1}$ (C−N).
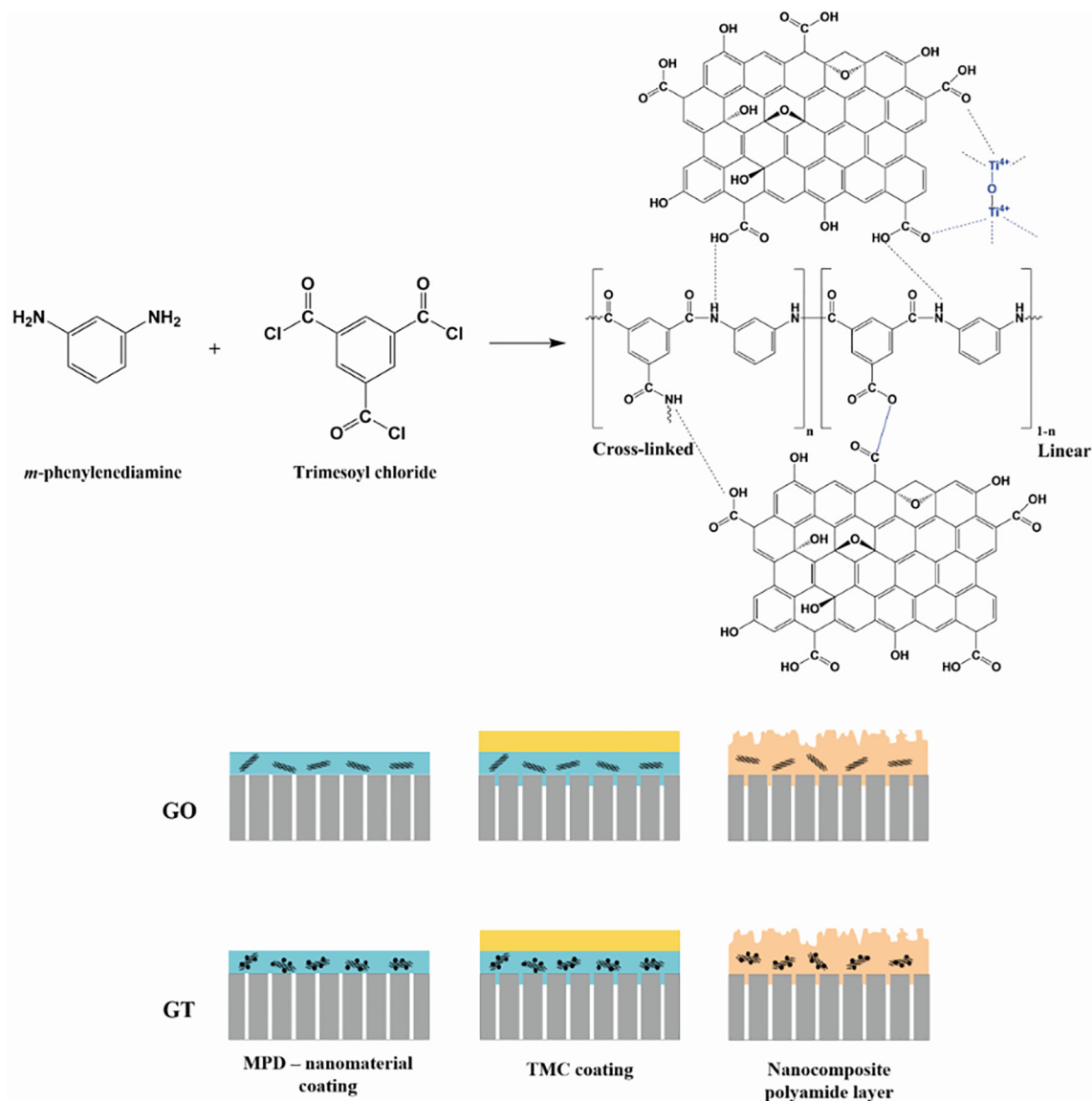
**Fig. 2.** Schematic diagram showing the interfacial polymerization reaction between MPD (containing nano-fillers GO and GT) and TMC. The resulting polyamide structure contains both cross-linked and linear portions.

availability of TMC for IP reaction. This results in a lesser degree of cross-linking in the polyamide layer.
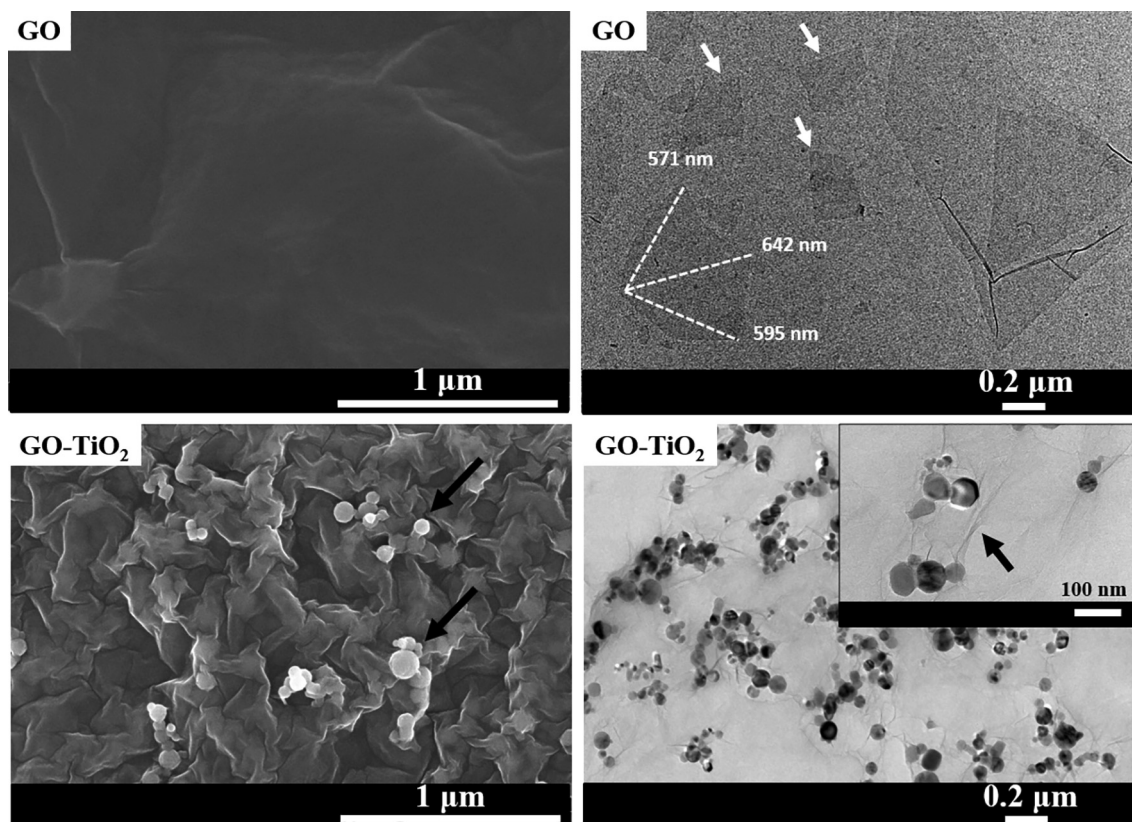
The interaction of GO nano-sheets and $TiO_2$ nanoparticles is via hydrogen bond between $Ti^{4+}$ and the carboxyl groups of GO [45,46]. Another mechanism reported in literature is the formation of Ti−O−C bonds by condensation of hydroxyl groups of $TiO_2$ and functional groups of GO [47,48].

### 3.1.2. Microscopy and contact angle

FE-SEM and TEM images of GO and GO-$TiO_2$ nanoparticles are presented in Fig. 3. It can be observed from the TEM images that the $TiO_2$ nanoparticles are more or less uniformly dispersed in GO solution. The average size of nanoparticles is ∼ 70 nm as calculated from the TEM images. The uniform dispersion of the $TiO_2$ nanoparticles in the graphene oxide matrix is of vital importance because otherwise, the particles will agglomerate and have a negative impact on the water vapor permeation.

Cross section images of GO and GT membranes are presented in Fig. 4. The polyamide layer is differentiated from PSf substrate by a yellow line. This line is not an accurate measure of the polyamide layer's starting point but just a guide to the eye. A thin and dense

polyamide layer can be clearly seen in the SEM images. The layer thickness is very hard to estimate because the surface roughness of the TFN membranes is higher than TFC membranes making it difficult to identify the edges. Furthermore, the polyamide layer starts from inside the surface pores of the PSf (as shown in schematic diagram of Fig. 2) and hence a clear boundary is hard to determine. SEM cross-section images of both the GO and GT membranes remain almost similar as a function of nano-filler concentration except at 2.0 wt%. At this concentration, the SEM cross-section image resembles that of a TFC membrane. For comparison, SEM image of a typical TFC membrane prepared using the same monomers is shown in Fig. S4 (Supplementary information). The change in cross-section morphology at higher concentration of GO and GT could be because of the agglomeration of nanoparticles. Nanoparticles readily agglomerate at higher concentrations because of their high surface energy and inter-particle interactions resulting in a diminished functionality. This can result in a hindrance for the MPD molecules to diffuse to the interface to form a polyamide layer. As a consequence, the nano-fillers are unevenly distributed across the polyamide film. Another explanation is that the GO nano-sheets are known to interact with the amines of MPD by hydrogen bonding, which results in interference in the interfacial polymerization reaction [44].

**Fig. 3.** FE-SEM and high resolution TEM images of GO nanosheets and GO-TiO$_2$ nano-filler. The TEM images reveal that the TiO$_2$ nanoparticles are uniformly attached to the GO sheets.

The reaction mechanism for the formation of polyamide layer on a membrane surface is well studied and reported in literature [10,11]. In the first step when MPD is allowed to flow through the hollow fibers, the near surface pores are completely wetted by the incoming aqueous phase monomer (schematic illustration in Fig. 2). These MPD molecules reside inside the pores and voids even after N$_2$ purging. The gas purging only removes the excess MPD solution from the surface of the membrane. In the next step when TMC flows through the hollow fibers, interfacial polymerization reaction occurs instantaneously on the surface. The solubility of amines is higher in organic solvent and therefore they rapidly diffuse to the organic front where they react with TMC. Thus, it can be said that MPD monomers that are residing in the pores and voids of the membrane erupt like a 'volcano' to react with TMC and form a polyamide nuclei which starts to grow laterally. These nuclei
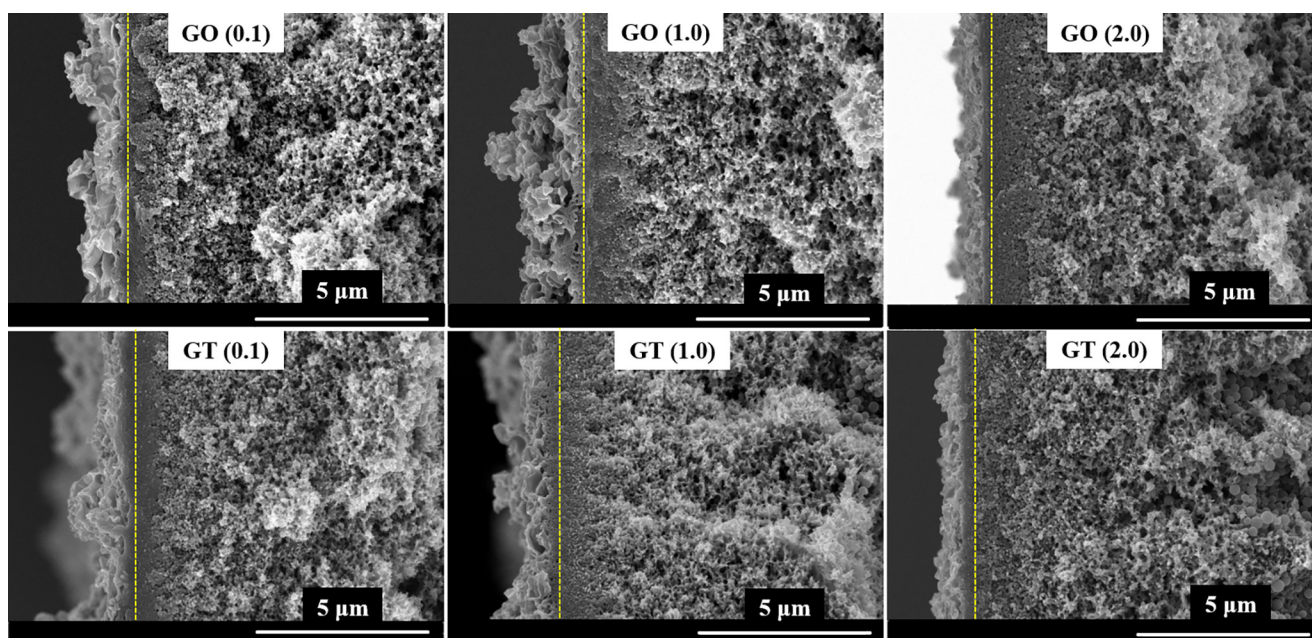


**Fig. 4.** Cross-section images of the TFN membranes with different loading of nano-fillers showing the polyamide layer morphology.

grow and combine with other nuclei to form a dense polyamide layer on the hollow fiber membrane surface. This mechanism gives rise to the characteristic ridge and valley type structure that can also be seen in the cross-section images of Fig. 4 and surface images of Fig. 5. However, the nanoparticles that are dispersed in the MPD solution do not diffuse towards the organic front but rather stay near the surface of the membrane. This means that the nanoparticles such as GO and GT are

embedded deep inside the polyamide layer. The excess of hydroxyl groups on the GO and GT nano-fillers form hydrogen bonds with the carbonyl groups of the polyamide membrane resulting in a stable attachment to the polyamide matrix. As a result, at relatively higher concentrations, the nano-fillers interfere with the IP reaction thereby reducing the cross-linking density of the PA film. This is proven to be true from the XPS results where the O/N ratio indicates the degree of
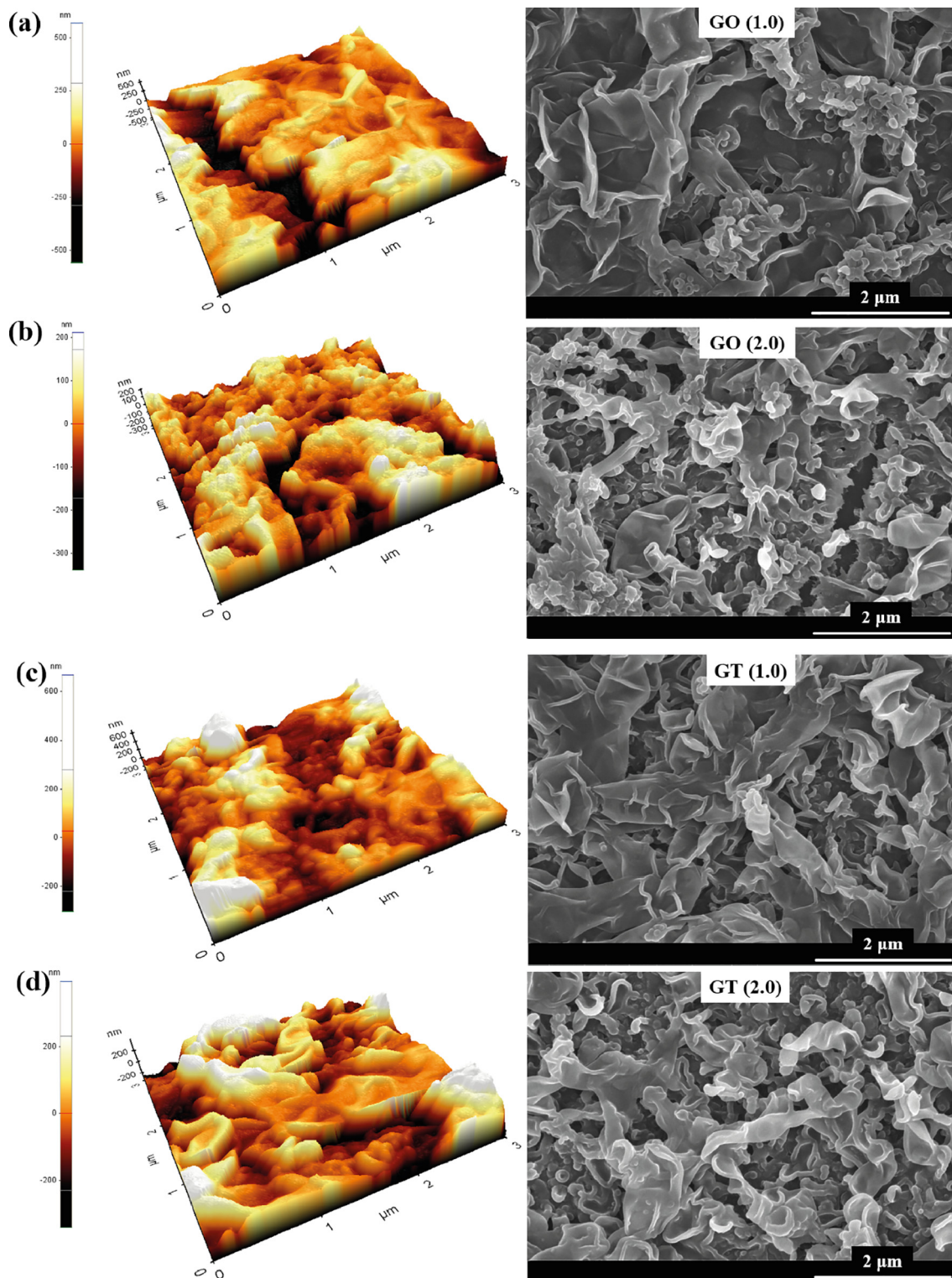


**Fig. 5.** AFM and surface SEM images of the TFN membranes with different loading of nano-fillers showing the typical leaf like morphology and the surface roughness profiles.

cross-linking.

The surface images of GO and GT based TFN membranes in Fig. 5 show a typical 'leaf like' morphology which is associated with the polyamide membranes prepared by interfacial polymerization [41]. FE-SEM images of all the nanocomposite membranes showed that the surface is fully coated with a dense and rough polyamide layer. The difference in the surface morphology is hard to see using SEM alone. Therefore, atomic force microscopy was conducted to get the surface roughness profiles of all the membranes. AFM images shown in Fig. 5 indicate the extent of surface roughness of both the GO and GT membranes. Average surface roughness increases with the increase in nano-fillers concentration in the polyamide layer up to 1.0 wt%. This trend is common for GO and GT based membranes. A further increase in concentration to 2.0 wt% of either the GO or GT causes the surface roughness to decrease again probably due to agglomeration effects as explained earlier. Surface roughness parameters and hydrophilicity measurements are summarized in Table 2.

In case of GO based TFN membranes, a maximum surface roughness of 669 nm was obtained for GO (1.0) with an average roughness of 100 nm. A highly rough surface is beneficial for improving the water vapor permeation through the membrane because it gives a larger surface area for the water vapor to adsorb. It means that a large volume of water vapor can pass through a rough membrane as compared to a smoother one. It will be shown in the permeation test results that a highly rough surface directly corresponds to a higher water vapor permeance. Similar trend was obtained in case of GT based membranes where a maximum roughness of 680 nm was obtained for GT (1.0). Interesting to note is that the GT based membranes had rougher surfaces on average than GO based membranes. As a result, it can be assumed that the GT based membranes shall have a higher water vapor permeance than GO.

The contact angles of both sets of TFN membranes also follow an interesting trend. It decreases till 1.0 wt% and then increases again at higher concentrations of nano-filler. However, it is important to mention that contrary to what is reported usually, the contact angle alone cannot be a true measure of membrane surface hydrophilicity. This is because the contact angle differs for a porous and smooth surface made of the same material. Therefore, surface roughness parameter has to be taken into account for giving estimations of surface hydrophilicity. As mentioned earlier, the modified Young-Dupre equation (Eq. (1)) gives the solid-liquid interfacial free energy which is a direct measure of surface hydrophilicity/wettability [49]. In this work, the surface hydrophilicity increases with the nano-fillers concentration. In case of GO based membranes, maximum value of 102 mJ/m$^2$ was achieved for GO (1.0) rendering it the most hydrophilic among this set. In comparison, the GT based membranes are more hydrophilic than GO. This is because the TiO$_2$ nanoparticles are bound with the GO sheets with hydrogen bonding that exists between hydroxyl groups on TiO$_2$ surface and the carbonyl groups on the GO sheets. Hydrogen bonding exists where there is excess hydroxyl and carbonyl moieties, both of which impart hydrophilic character. Higher concentration of GT in the polyamide membrane without agglomeration, i.e. GT (1.0), gives a highly hydrophilic and rough surface. Also, the infrared spectroscopy revealed the presence of carboxyl groups in the PA layer which is itself responsible for imparting hydrophilic character. The maximum solid-liquid interfacial free energy that can be achieved for a complete wetting is 2γ$_L$, twice the surface tension of water (145.6 mJ/m$^2$). In case of GT (1.0), the maximum value of $-\Delta G_{SL}$ is 1.65γ$_L$ (120 mJ/m$^2$) which proves that the membrane surface is highly hydrophilic. However, following the same trend as the surface roughness, hydrophilicity of the membrane also decreases at 2.0 wt% GO and GT nano-fillers loading.

### 3.1.3. X-ray photoelectron spectroscopy (XPS) analysis

XPS was used to analyze the elemental composition and the bonding chemistry of the top surface of nanocomposite membranes. XPS is a highly surface sensitive technique and can only penetrate to a

maximum of 5 nm inside the surface [50]. As explained earlier, since the nano-fillers are embedded deep inside the polyamide layer, the surface scan cannot show their existence in the polyamide layer. The atomic composition of the polyamide top layer of TFN based membranes is presented in Table 3. Carbon, nitrogen, and oxygen are the main elements detected since they are the backbone of the polyamide layer. Hydrogen composition cannot be determined using XPS and, therefore, is absent from the table. Understandably, the PSf substrate does not contain nitrogen, instead, 7.2 atom % Sulphur was detected. The coating completely covered the PSf substrate and hence, the composition of GO (1.0) and GT (1.0) membranes is purely that of the modified polyamide layer.

O/N ratio gives an indication of the degree of cross-linking in the polyamide layer. An O/N ratio of 1 corresponds to a fully cross-linked polyamide, which means that each Oxygen atom is chemically bonded to a Nitrogen atom (n = 1 in Fig. 2). While an O/N ratio of 2 indicates a linear polyamide with no cross-linking (n = 0 in Fig. 2) [36]. All the membrane prepared in this work have O/N ratios between 1 and 2. This means that the membranes are not fully cross-linked but have both cross-linked and linear parts. However, the O/N ratios are closer to 1 meaning that the polyamide layer has more cross-links than linear portions. Another significant observation is that GO (1.0) is slightly more cross-linked than GT (1.0). Since the polyamide is not fully cross-linked (O/N > 1) and the oxygen content increases from GO (1.0) to GT (1.0), it can be concluded that the C–N bonds were hydrolyzed to form carboxyl groups. This was confirmed by the FTIR results verifying the presence of carboxyl groups in TFN membranes prepared using higher concentrations of nano-fillers. In Fig. 1, a small absorption peak at 1760 cm$^{-1}$ for GO (2.0) and GT (2.0) was attributed to the C=O stretching of the carboxyl group. Similar findings were reported by Do et al. [51]. Carboxyl and hydroxyl groups are also known to increase wettability of the membrane. The increase in hydrophilicity from GO (1.0) to GT (1.0) could also be linked to an increase in carboxyl functional groups in the membrane.

Further information regarding the chemical bonding of Carbon, Oxygen, and Nitrogen atoms was obtained by deconvoluting the high resolution XPS spectra of the said atoms. The high resolution XPS scans of C (1s), N (1s), and O (1s) are shown in Fig. 6. Peaks were fitted to determine the binding energy shifts (δ$_{BE}$) of the atoms. Three distinct peaks were observed for C (1s) in both the GO and GT based polyamide membranes. The major peak at 284.4 eV (δ$_{BE}$ = 0) is assigned to Carbon atoms without adjacent electron withdrawing groups. These can be either aliphatic C–C and/or C–H bonds. A second peak appears at 285.6 eV (δ$_{BE}$ = 1.2 eV) which is due to the Carbon atoms that are bonded to a weak electron withdrawing group (C–O). A positive binding energy shift always indicates that the Carbon atom is bonded to

**Table 2**
Surface roughness parameters and contact angle measurements of GO and GT based TFN membranes. $R_a$ = average surface roughness, $R_{max}$ = maximum surface roughness, $R_q$ = root mean square surface roughness, $\Delta$ = relative surface area, and $-\Delta G_{SL}$ = solid-liquid interfacial free energy.

| Membrane | $R_a$ (nm) | $R_{max}$ (nm) | $R_q$ (nm) | $\Delta$ (-) | Contact angle (°) | $-\Delta G_{SL}$ (mJ/m$^2$) |
|---|---|---|---|---|---|---|
| GO (0.05) | 23 | 109 | 29 | 1.06 | 88 ± 3 | 75 |
| GO (0.1) | 16 | 127 | 21 | 1.61 | 87 ± 2 | 75 |
| GO (0.2) | 97 | 436 | 122 | 1.80 | 59 ± 2 | 94 |
| GO (0.5) | 108 | 482 | 136 | 1.92 | 49 ± 1 | 98 |
| GO (1.0) | 100 | 669 | 133 | 1.64 | 49 ± 2 | 102 |
| GO (2.0) | 58 | 212 | 75 | 1.72 | 53 ± 1 | 98 |
| GT (0.05) | 24 | 117 | 34 | 1.17 | 72 ± 4 | 92 |
| GT (0.1) | 59 | 230 | 73 | 2.19 | 56 ± 1 | 91 |
| GT (0.2) | 96 | 500 | 123 | 1.67 | 53 ± 2 | 99 |
| GT (0.5) | 97 | 567 | 129 | 1.71 | 50 ± 2 | 100 |
| GT (1.0) | 130 | 680 | 169 | 1.13 | 44 ± 1 | 120 |
| GT (2.0) | 93 | 395 | 118 | 1.57 | 73 ± 2 | 86 |

**Table 3**
Elemental composition of PSf substrate and the TFN membranes containing GO and GT nano-fillers.

| Membrane | Atomic % | | | |
|---|---|---|---|---|
| | C | N | O | O/N ratio |
| PSf substrate | 70.4 | 0 | 22.4 | – |
| GO (1.0) | 75.9 | 10.3 | 12 | 1.17 |
| GT (1.0) | 75 | 10.7 | 13.1 | 1.22 |

highly electronegative atoms. A third small peak appeared at $\delta_{BE} = 3.5$ eV (287.9 eV) which is assigned to the Carbon atoms bonded to strongly electron withdrawing groups such as O=C−O in carboxylic and O=C−N in amide groups [52]. The XPS results of C (1s) are in accordance with the data obtained from ATR-FTIR absorption peaks confirming the presence of amide, carboxyl and hydroxyl groups.

The deconvolution of high resolution XPS scan of O (1s) reveals 2 major peaks; carbonyl oxygen (O=C−O, O=C−N) at 531.2 eV, and carboxylic oxygen (O=C−O) at 532.6 eV. The intensity of carboxyl peak in GT was higher than GO based membranes indicating a comparatively lesser degree of cross-linking in the former due to the bonding of GT with PA layer. This is in accordance with relatively higher O/N values (less cross-links) for GT membranes shown in Table 3. The XPS data did not show any Ti in the atomic composition of the polyamide layer because the depth of penetration for XPS is around 5 – 6 nm. It confirms our earlier hypothesis that the nano-fillers GO and GT are embedded deep inside the polyamide layer rather than residing near the surface. The XPS scan of N (1s) revealed only one peak at 400 eV after deconvoluting the data. This peak is assigned to the amide Nitrogen which is expected because N only exists in amide bond in the polymer membrane.

### 3.1.4. Thermal gravimetric analysis (TGA)

Thermal stability of the TFN membranes was analyzed by TGA and the results are shown in Fig. 7. The nanocomposite membranes showed a typical three step degradation process. In the first step (I), water and volatile matter evaporates in the temperature range 25–150 °C. The second step (II) involves thermochemical decomposition of polymer chains that occurs between 150 and 500 °C. The decomposition in this stage happens because the sulfone chains start to break after 250 °C due to the loss of sulfonic acid groups [53]. In the last step (III), the residues and degraded matter is carbonized. The weight loss in the initial step is around 8% for PSf substrate as compared to 2.7% for the TFN membranes. By the end of second step decomposition, GT based membranes have only lost 20% weight as compared to 23% for GO based membranes. This indicates that GT membranes are slightly better in terms of
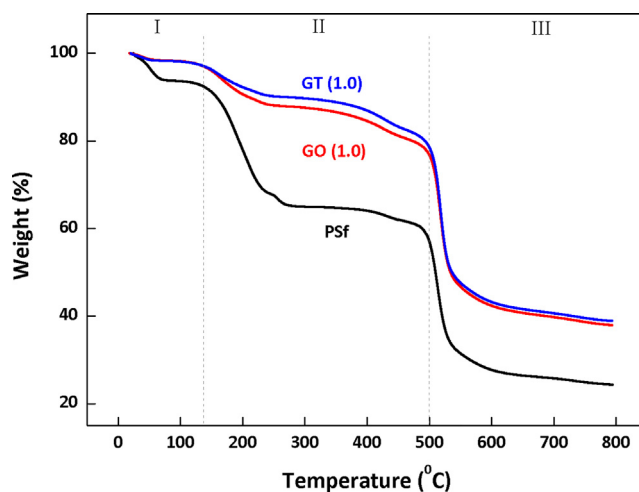


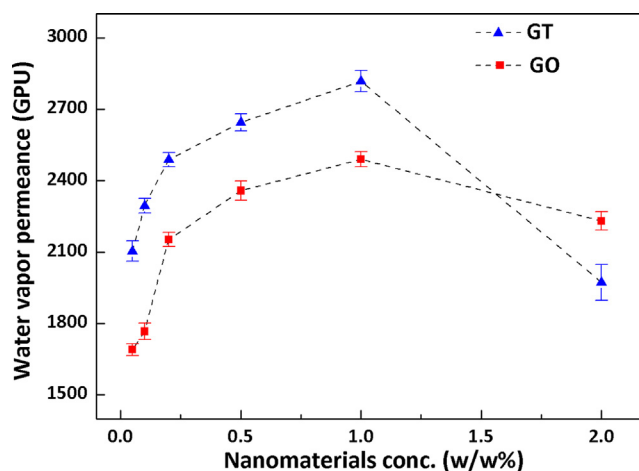**Fig. 7.** TGA thermograms of PSf substrate, GO (1.0) and GT (1.0) TFN membranes.



**Fig. 8.** Water vapor permeance of the GO and GT based TFN membranes as a function of the nano-fillers concentration. Permeation experiments were conducted at 30 °C, 1000 cm³/min feed flow rate, 3 kg-f/cm² operating pressure, 75–80% relative humidity.

thermal stability than the GO membranes. The residual matter at the end of the test was approximately 39% and 38% for TFN membranes while only 24% for PSf substrate. The increase in thermal stability of TFN membranes is because of the decrease in chain mobility due to the
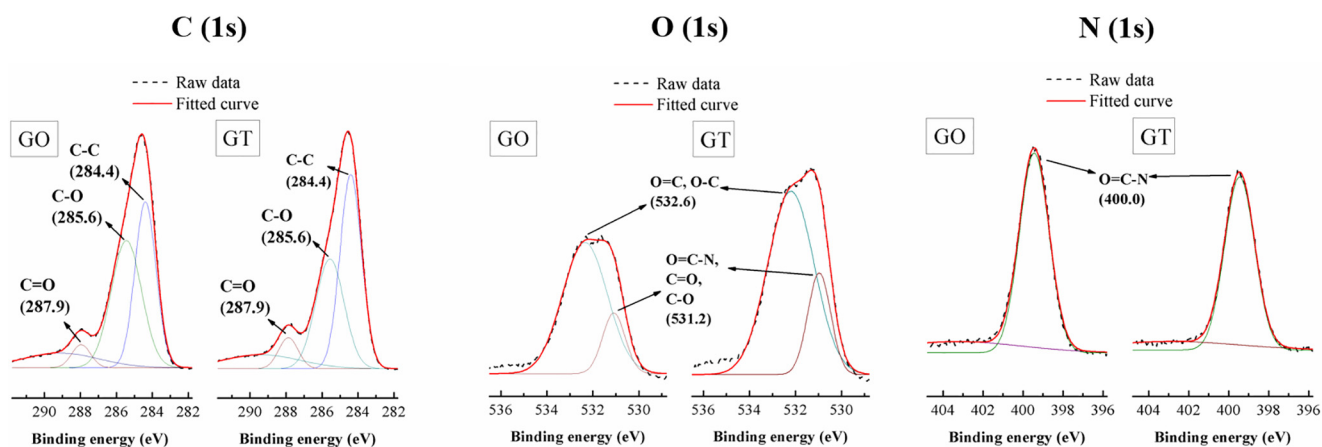


**Fig. 6.** High resolution XPS spectra and peak deconvolution of C (1s), O (1s), and N (1s) of GO and GT based polyamide membranes.
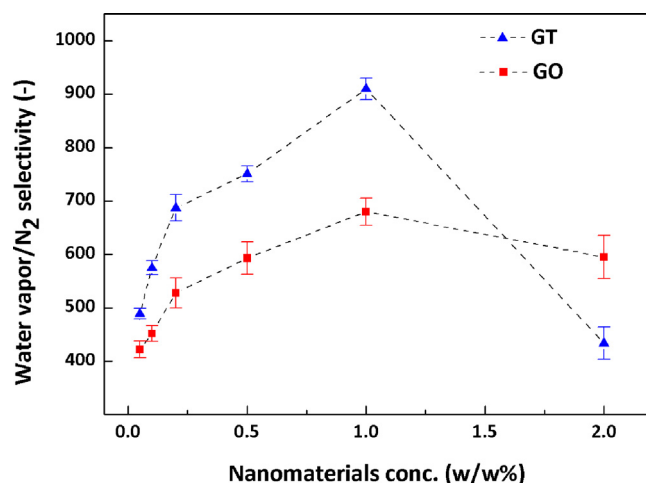
**Fig. 9.** Water vapor/N$_2$ selectivity of the GO and GT based TFN membranes as a function of the nano-fillers concentration.

presence of nanoparticles.

### 3.2. Mixed gas separation performance

Gas transport in dense membranes is explained by the 'solution-diffusion' mechanism. The first step involves the sorption of gas molecules on the membrane surface. In the second step, gas molecules diffuse through the membrane and finally, in the third step they desorb on the permeate side. As the name suggests, the solubility and diffusivity of gas molecules is very important in determining the permeability of species. Solubility is a thermodynamic property that gives the amount of species sorbed on the membrane surface. On the other hand, diffusivity is a kinetic parameter and dictates how fast a molecule will be transported through the membrane. Diffusivity is mostly related to the kinetic diameter of the gases. The kinetic diameter of N$_2$ is 3.64 Å and that of water vapor is 2.65 Å [54]. Intuitively, water vapor will diffuse faster than Nitrogen gas upon applying pressure across the membrane. However, diffusivity of the gas molecule alone cannot accurately determine the permeability because a larger molecule, such as CO$_2$, can also diffuse faster in a rubbery polymer because of its high solubility. Solubility of a gas molecule is determined by its solubility coefficient. Since it is the first step in solution-diffusion mechanism, a membrane surface that is modified to achieve high sorption of a certain gas molecule will result in a high permeability of that component. Therefore, to selectively remove water vapor from N$_2$ gas stream, a hydrophilic surface will ensure maximum sorption of water vapor and hence, a high water vapor permeance. One of the aim of this work was to have a

highly hydrophilic polyamide layer on the PSf support for increasing the water vapor permeance. AFM and contact angle measurements already verified the presence of a hydrophilic nanocomposite membrane on the PSf support.

It is already established that the TFN membranes' hydrophilicity increases with the increase in GO and GT nano-fillers concentration (up to 1.0% loading). This directly implies that the water vapor permeance shall also follow the same trend. Figs. 8 and 9 show the water vapor permeance and selectivity as a function of nano-fillers concentration.

A thin film composite membrane without the nanoparticles was also prepared using 2 wt% MPD and 0.2 wt% TMC. This TFC membrane was used as a reference to compare the TFN membrane performance. The water vapor permeance and selectivity of the TFC membrane was 1360 GPU and 378, respectively.

When compared with each other, the two types of nano-fillers that are added to the polyamide layer i.e. GO and GT, show a similar trend of permeance as a function of concentration. Water vapor permeance increases with the nano-fillers concentration and achieves a maximum before dropping again. The two types of nano-fillers and their effect on water vapor permeation are discussed separately.

#### 3.2.1. Graphene oxide based TFN Membranes

Addition of GO in the polyamide layer significantly affected the water vapor permeance and selectivity of the TFN membranes. From 1360 GPU for TFC membrane, the permeance increased to 1690 GPU for GO (0.05). The water vapor permeance continues to increase with the addition of graphene oxide till GO (1.0), where it achieves a maximum permeance and selectivity of 2500 GPU and 680, respectively. A further increase in GO concentration causes the nano-fillers to agglomerate rendering them rather ineffective. This is validated by looking at the water vapor permeance of GO (2.0) which drops down to 2230 GPU. Similar trend was observed for the water vapor/N$_2$ selectivity which drops from 680 to 595 (Fig. 9). GO nano-sheets have a very high specific surface area. These sheets are embedded deep inside the polyamide layer where they form a 2D capillary network. This network of GO enhances the water vapor transport by providing ultrafast permeation paths. The existence of water channels coupled with an increased surface roughness of the polyamide nanocomposite membrane provides a larger surface area for the water vapor to adsorb.

Increase in vapor/N$_2$ selectivity with the increase in concentration of GO is primarily due to the increase in water vapor permeance. Nitrogen gas permeance is not affected by the increasing concentration of GO which means that the permeance is mostly governed by 'solution' in this case. The permeation performance starts to deteriorate at higher concentrations of GO. This can be due to the stacking of GO nano-sheets on top of each other and thus interfering in the interfacial polymerization reaction. This results in a PA layer that is less cross-linked

**Table 4**

Comparison of water vapor permeation performance of membranes prepared in this work with state-of-the-art membranes reported in literature.

| Membrane | Operating temperature (°C) | Water vapor permeance (GPU) | Water vapor/N$_2$ selectivity | Refs. |
|---|---|---|---|---|
| PEI/PEBAX®1657 | 21 | 1800 | 1800 | [55] |
| Ni/NaA | 32 | 20,042 | 178 | [56] |
| Stabilized Triethylene glycol | 15–30 | 223 | 2000 | [57] |
| [Emim][Tf2N] ionic liquid | 31 | 635 | 3840 | [58] |
| PSf/MOF modified composite membrane | 30 | 2244 | 542 | [59] |
| PSf/MPD-TMC | 30 | 1500 | 500 | [60] |
| PSF/Nafion-IL-SiO$_2$ composite membrane | 30 | 2131 | 25 | [61] |
| PSF/SiO$_2$ composite membrane | 30 | 2125 | 581 | [39] |
| PSF/Hydroxylated TiO$_2$ composite membrane | 30 | 1396 | 510 | [62] |
| PSf/Carboxylated TiO$_2$ composite membrane | 30 | 1340 | 486 | [40] |
| PSf/sb-cyclodextrin composite membrane | 30 | 1597 | 503 | [63] |
| PSF/ETS-0.4 composite membrane | 30 | 1377 | 346 | [64] |
| PSF/βCD-Fe$_3$O$_4$ nanoparticles composite membrane | 30 | 2237 | 774 | [65] |
| PSF/GO (1.0) nanocomposite membrane | 30 | 2500 | 680 | This work |
| PSF/GT (1.0) nanocomposite membrane | 30 | 2820 | 910 | This work |

and has smoother surfaces as confirmed by AFM data and Fig. 5 (b).

### 3.2.2. GO-TiO$_2$ based TFN Membranes

The graph of GT based membranes follows a similar trend as GO. However, in comparison to GO, the water vapor permeance and selectivity is greater for GT based membranes. At the same nano-filler concentration of 0.05 wt%, the water vapor permeance of GT is 2104 GPU as compared to 1690 GPU of GO. This 25% increase was already predicted by surface roughness parameters and the interfacial free energy of GT membranes (Table 2). GT based membranes are more hydrophilic and have a larger surface area coupled with a lesser degree of cross-linking as compared to the GO membranes. A lower degree of cross-linking results in more free volume consequently increasing the water vapor transport.

The water vapor permeance increases with the increase in GT concentration till a maximum of 2820 GPU is obtained for GT (1.0). A further increase in GT concentration causes the permeance to immediately drop to 1973 GPU, constituting a 30% decline. This can be attributed to the increase in aggregation of the nano-fillers at such a large concentrations triggered by TiO$_2$ nanoparticles ($\sim$70 nm). These aggregates interfere strongly with IP reaction and form defects in the selective layer thus having a negative impact on the transport properties of the membrane. Also, at higher concentration, the agglomeration effects render these nanomaterials ineffective and the membrane behaves as a defective membrane. This can explain the decrease in both the permeance as well as selectivity for GO (2.0) and GT (2.0). It has been widely reported that the nanomaterials concentration in the PA layer always has a limit. Increase in concentration from that limit negatively affects is found on the separation performance of the membranes [34,44]. Same trend is followed by the vapor/N$_2$ selectivity where it reaches a maximum of 910 for GT (1.0) and then drop down to 434 for GT (2.0). This pronounced decrease in selectivity is due to the increase in Nitrogen permeance and decrease in water vapor permeance caused by the defects in the membrane. Membrane morphology shown in Fig. 4 confirms that at higher loading of nano-fillers, the membrane structure resembles a TFC membrane (Fig. S4 Supplementary Information). Nevertheless, it is pertinent to mention that a water vapor permeance in excess of 2800 GPU with vapor/N$_2$ selectivity over 900 is a remarkable result for a TFN membrane for water vapor separation. The membranes prepared in this work are compared with the state-of-the-art TFN membranes and the results are reported in Table 4. Only the mixed vapor/gas permeances are mentioned in this table. The membranes prepared in this work have higher permeance and selectivity for water vapor over N$_2$.

The inclusion of graphene oxide and graphene oxide-TiO$_2$ nano-fillers in the polyamide membrane not only increases the water permeation performance of the membranes but also strengthens the PA layer. These nanomaterials open up more topics for further research on nanocomposite membranes for water based membrane applications.

### 4. Conclusions

Thin film nanocomposite membranes were prepared using graphene oxide (GO) and graphene oxide-TiO$_2$ (GT) composites as filler materials for the polyamide layer. The nano-fillers were added to the aqueous phase monomer in different concentrations. The interfacial polymerization reaction with the organic phase monomer resulted in a dense polyamide nanocomposite membrane on a porous PSf hollow fiber support. It was found that GO and GT are bonded to the polyamide layer via hydrogen bonds. This results are a stable attachment of the nano-fillers to the PA layer. Also, the GT combination has more hydrogen bonds within the nanomaterial and also with the PA layer. The surface of PA appeared very rough with a characteristic ridge and valley like structure. It was found that GT based membranes had higher surface roughness as well as excellent hydrophilicity as compared to GO because of the hydrogen bonding and presence of excess carboxyl

groups in the PA layer. XPS results indicated that GT based membranes had a lesser degree of cross-linking than GO because of the interference in polymerization reaction. The water vapor permeance and selectivity increased with the increase in nano-fillers concentration till 1.0 wt%. Further increase in the nano-filler concentration resulted in a sharp decline in the membrane performance due to agglomeration effects. A highly hydrophilic and rough membrane surface with lesser degree of cross-linking makes GT based membranes far better for water vapor separation applications. The membranes prepared in this work show better performance in terms of water vapor permeance (2820 GPU) and vapor/N$_2$ selectivity (9 1 0) as compared (with the mixture gas) to the other TFN membranes reported in literature.

### Declaration of Competing Interest

There is no conflict of interest to declare.

### Appendix A. Supplementary data

Supplementary data to this article can be found online at https://doi.org/10.1016/j.cej.2019.05.122.

### References

[1] J.T. Kiehl, K.E. Trenberth, Earth's annual global mean energy budget, Bull. Am. Meteorol. Soc. 78 (1997) 197–208, https://doi.org/10.1175/15200477(1997)078<0197:EAGMEB>2.0.CO;2.

[2] A.E. Dessler, M.R. Schoeberl, T. Wang, S.M. Davis, K.H. Rosenlof, Stratospheric water vapor feedback, Proc. Natl. Acad. Sci. 110 (2013) 18087–18091, https://doi.org/10.1073/pnas.1310344110.

[3] J. Woods, Membrane processes for heating, ventilation, and air conditioning, Renew. Sustain. Energy Rev. 33 (2014) 290–304, https://doi.org/10.1016/j.rser.2014.01.092.

[4] K. Kneifel, S. Nowak, W. Albrecht, R. Hilke, R. Just, K.V. Peinemann, Hollow fiber membrane contactor for air humidity control: modules and membranes, J. Membr. Sci. 276 (2006) 241–251, https://doi.org/10.1016/j.memsci.2005.09.052.

[5] M. Strand, J. Pagels, A. Szpila, A. Gudmundsson, E. Swietlicki, M. Bohgard, M. Sanati, Fly ash penetration through electrostatic precipitator and flue gas condenser in a 6 MW biomass fired boiler, Energy Fuels 16 (2002) 1499–1506, https://doi.org/10.1021/ef020076b.

[6] H. Sijbesma, K. Nymeijer, R. van Marwijk, R. Heijboer, J. Potreck, M. Wessling, Flue gas dehydration using polymer membranes, J. Membr. Sci. 313 (2008) 263–276, https://doi.org/10.1016/j.memsci.2008.01.024.

[7] J.E. Cadotte, R.J. Petersen, R.E. Larson, E.E. Erickson, A new thin-film composite seawater reverse osmosis membrane, Desalination 32 (1980) 25–31, https://doi.org/10.1016/S0011-9164(00)86003-8.

[8] J. Albo, J. Wang, T. Tsuru, Gas transport properties of interfacially polymerized polyamide composite membranes under different pre-treatments and temperatures, J. Membr. Sci. 449 (2014) 109–118, https://doi.org/10.1016/j.memsci.2013.08.026.

[9] Y. Song, P. Sun, L. Henry, B. Sun, Mechanisms of structure and performance controlled thin film composite membrane formation via interfacial polymerization process, J. Membr. Sci. 251 (2005) 67–79, https://doi.org/10.1016/j.memsci.2004.10.042.

[10] A.K. Ghosh, B.H. Jeong, X. Huang, E.M.V. Hoek, Impacts of reaction and curing conditions on polyamide composite reverse osmosis membrane properties, J. Membr. Sci. 311 (2008) 34–45, https://doi.org/10.1016/j.memsci.2007.11.038.

[11] G.Y. Chai, W.B. Krantz, Formation and characterization of polyamide membranes via interfacial polymerization, J. Membr. Sci. 93 (1994) 175–192, https://doi.org/10.1016/0376-7388(94)80006-5.

[12] B.H. Jeong, E.M.V. Hoek, Y. Yan, A. Subramani, X. Huang, G. Hurwitz, A.K. Ghosh, A. Jawor, Interfacial polymerization of thin film nanocomposites: a new concept for reverse osmosis membranes, J. Membr. Sci. 294 (2007) 1–7, https://doi.org/10.1016/j.memsci.2007.02.025.

[13] V. Dusastre, A.S. Aricò, P. Bruce, B. Scrosati, J.-M. Tarascon, W.v. Schalkwijk, Nanostructured materials for advanced energy conversion and storage devices, Nature Publishing Group, Mater. Sustain. Energy (2012) 148–159, https://doi.org/10.1142/9789814317665_0022.

[14] Y. Gao, Z. Qiao, S. Zhao, Z. Wang, J. Wang, In situ synthesis of polymer grafted ZIFs and application in mixed matrix membrane for $CO_2$ separation, J. Mater. Chem. A 6 (2018) 3151–3161, https://doi.org/10.1039/c7ta10322k.

[15] A.A. Shamsabadi, F. Seidi, E. Salehi, M. Nozari, A. Rahimpour, M. Soroush, Efficient $CO_2$ removal using novel mixed-matrix membranes with modified $TiO_2$ nanoparticles, J. Mater. Chem. A 5 (2017) 4011–4025, https://doi.org/10.1039/c6ta09990d.

[16] A. Dehghani Kiadehi, A. Rahimpour, M. Jahanshahi, A.A. Ghoreyshi, Novel carbon nano-fibers (CNF)/polysulfone (PSf) mixed matrix membranes for gas separation, J. Ind. Eng. Chem. 22 (2015) 199–207, https://doi.org/10.1016/j.jiec.2014.07.011.

[17] L. Ansaloni, Y. Zhao, B.T. Jung, K. Ramasubramanian, M.G. Baschetti, W.S.W. Ho, Facilitated transport membranes containing amino-functionalized multi-walled carbon nanotubes for high-pressure $CO_2$ separations, J. Membr. Sci. 490 (2015) 18–28, https://doi.org/10.1016/j.memsci.2015.03.097.

[18] J. Ahn, W.J. Chung, I. Pinnau, M.D. Guiver, Polysulfone/silica nanoparticle mixed-matrix membranes for gas separation, J. Membr. Sci. 314 (2008) 123–133, https://doi.org/10.1016/j.memsci.2008.01.031.

[19] T. Rodenas, I. Luz, G. Prieto, B. Seoane, H. Miro, A. Corma, F. Kapteijn, F.X. Llabrés I Xamena, J. Gascon, Metal-organic framework nanosheets in polymer composite materials for gas separation, Nat. Mater. 14 (2015) 48–55, https://doi.org/10.1038/nmat4113.

[20] C. Kong, H. Du, L. Chen, B. Chen, Nanoscale MOF/organosilica membranes on tubular ceramic substrates for highly selective gas separation, Energy Environ. Sci. 10 (2017) 1812–1819, https://doi.org/10.1039/c7ee00830a.

[21] K.C. Wong, P.S. Goh, A.F. Ismail, Highly permeable and selective graphene oxide-enabled thin film nanocomposite for carbon dioxide separation, Int. J. Greenh. Gas Control. 64 (2017) 257–266, https://doi.org/10.1016/j.ijggc.2017.08.005.

[22] H. Li, X. Ding, Y. Zhang, J. Liu, Porous graphene nanosheets functionalized thin film nanocomposite membrane prepared by interfacial polymerization for $CO_2/N_2$ separation, J. Membr. Sci. 543 (2017) 58–68, https://doi.org/10.1016/j.memsci.2017.08.046.

[23] C.M. Costa, M. Kundu, J.C. Dias, J. Nunes-Pereira, G. Botelho, M.M. Silva, S. Lanceros-Méndez, Mesoporous poly(vinylidene fluoride-co-trifluoroethylene) membranes for lithium-ion battery separators, Electrochim. Acta 301 (2019) 97–106.

[24] N. Sarabchi, S.M.S. Mahmoudi, M. Yari, A. Farzi, Exergoeconomic analysis and optimization of a novel hybrid cogeneration system: high-temperature proton exchange membrane fuel cell/Kalina cycle, driven by solar energy, Energy. Convers. Manage. 190 (2019) 14–33.

[25] D. Li, H. Zhang, X. Li, Porous polyetherimide membranes with tunable morphology for lithium-ion battery, J. Membr. Sci. 565 (2018) 42–49.

[26] V.H. Nguyen, D.H. Lee, S.Y. Baek, Y.H. Kim, Recycling different eggshell membranes for lithium-ion battery, Mater. Lett. 228 (2018) 504–508.

[27] Y. Shi, C. Eze, B. Xiong, W. He, H. Zhang, T.M. Lim, A. Ukil, J. Zhao, Recent development of membrane for vanadium redox flow battery applications: a review, Appl. Energy 238 (2019) 202–224.

[28] M.I. Baig, P.G. Ingole, W.K. Choi, J. deok Jeon, B. Jang, J.H. Moon, H.K. Lee, Synthesis and characterization of thin film nanocomposite membranes incorporated with surface functionalized Silicon nanoparticles for improved water vapor permeation performance, Chem. Eng. J. 308 (2017) 27–39, https://doi.org/10.1016/j.cej.2016.09.033.

[29] P.G. Ingole, M.I. Baig, W.K. Choi, H.-K. Lee, Synthesis and characterization of polyamide/polyester thin-film nanocomposite membranes achieved by functionalized $TiO_2$ nanoparticles for water vapor separation, J. Mater. Chem. A 4 (2016) 5592–5604, https://doi.org/10.1039/c6ta00100a.

[30] P.G. Ingole, R.R. Pawar, M.I. Baig, J.D. Jeon, H.K. Lee, Thin film nanocomposite (TFN) hollow fiber membranes incorporated with functionalized acid-activated bentonite (ABn-NH) clay: towards enhancement of water vapor permeance and selectivity, J. Mater. Chem. A 5 (2017) 20947–20958, https://doi.org/10.1039/c7ta04945e.

[31] K.P. Lee, H. Leese, D. Mattia, Water flow enhancement in hydrophilic nanochannels, Nanoscale 4 (2012) 2621–2627, https://doi.org/10.1039/c2nr30098b.

[32] L. Wu, L. Liu, B. Gao, R. Muñoz-Carpena, M. Zhang, H. Chen, Z. Zhou, H. Wang, Aggregation kinetics of graphene oxides in aqueous solutions: experiments, mechanisms, and modeling, Langmuir 29 (2013) 15174–15181, https://doi.org/10.1021/la404134x.

[33] S. Xia, L. Yao, Y. Zhao, N. Li, Y. Zheng, Preparation of graphene oxide modified polyamide thin film composite membranes with improved hydrophilicity for natural organic matter removal, Chem. Eng. J. 280 (2015) 720–727, https://doi.org/10.1016/j.cej.2015.06.063.

[34] G.S. Lai, W.J. Lau, P.S. Goh, A.F. Ismail, Y.H. Tan, C.Y. Chong, R. Krause-Rehberg, S. Awad, Tailor-made thin film nanocomposite membrane incorporated with graphene oxide using novel interfacial polymerization technique for enhanced water separation, Chem. Eng. J. 344 (2018) 524–534, https://doi.org/10.1016/j.cej.2018.03.116.

[35] J. Yin, G. Zhu, B. Deng, Graphene oxide (GO) enhanced polyamide (PA) thin-film nanocomposite (TFN) membrane for water purification, Desalination 379 (2016) 93–101, https://doi.org/10.1016/j.desal.2015.11.001.

[36] L. Chen, N. Li, Z. Wen, L. Zhang, Q. Chen, L. Chen, P. Si, J. Feng, Y. Li, J. Lou, L. Ci, Graphene oxide based membrane intercalated by nanoparticles for high performance nanofiltration application, Chem. Eng. J. 347 (2018) 12–18, https://doi.org/10.1016/J.CEJ.2018.04.069.

[37] P. Gao, D.D. Sun, Ultrasonic preparation of hierarchical graphene-oxide/$TiO_2$ composite microspheres for efficient photocatalytic hydrogen production, Chem. Ann. Asian J. 8 (2013) 2779–2786, https://doi.org/10.1002/asia.201300565.

[38] R.N. Wenzel, Surface Roughness and Contact Angle, J. Phys. Colloid Chem. 53 (1949) 1466–1467, https://doi.org/10.1021/j150474a015.

[39] M.I. Baig, P.G. Ingole, J. deok Jeon, S.U. Hong, W.K. Choi, B. Jang, H.K. Lee, Water vapor selective thin film nanocomposite membranes prepared by functionalized Silicon nanoparticles, Desalination 451 (2019) 59–71, https://doi.org/10.1016/j.desal.2017.06.005.

[40] M.I. Baig, P.G. Ingole, W.K. Choi, S.R. Park, E.C. Kang, H.K. Lee, Development of carboxylated $TiO_2$ incorporated thin film nanocomposite hollow fiber membranes for flue gas dehydration, J. Membr. Sci. 514 (2016) 622–635, https://doi.org/10.1016/j.memsci.2016.05.017.

[41] C.Y. Tang, Y.N. Kwon, J.O. Leckie, Effect of membrane chemistry and coating layer on physiochemical properties of thin film composite polyamide RO and NF membranes. I. FTIR and XPS characterization of polyamide and coating layer chemistry, Desalination 242 (2009) 149–167, https://doi.org/10.1016/j.desal.2008.04.003.

[42] D.C. Marcano, D.V. Kosynkin, J.M. Berlin, A. Sinitskii, Z. Sun, A. Slesarev, L.B. Alemany, W. Lu, J.M. Tour, Improved synthesis of graphene oxide, ACS Nano 4 (2010) 4806–4814, https://doi.org/10.1021/nn1006368.

[43] A.P. Rao, S.V. Joshi, J.J. Trivedi, C.V. Devmurari, V.J. Shah, Structure-performance correlation of polyamide thin film composite membranes: effect of coating conditions on film formation, J. Membr. Sci. 211 (2003) 13–24, https://doi.org/10.1016/S0376-7388(02)00305-8.

[44] M.E.A. Ali, L. Wang, X. Wang, X. Feng, Thin film composite membranes embedded with graphene oxide for water desalination, Desalination 386 (2016) 67–76, https://doi.org/10.1016/j.desal.2016.02.034.

[45] Y. Gao, M. Hu, B. Mi, Membrane surface modification with $TiO_2$-graphene oxide for enhanced photocatalytic performance, J. Membr. Sci. 455 (2014) 349–356, https://doi.org/10.1016/j.memsci.2014.01.011.

[46] S. Yu, X. Wang, R. Zhang, T. Yang, Y. Ai, T. Wen, W. Huang, T. Hayat, A. Alsaedi, X. Wang, Complex roles of solution chemistry on graphene oxide coagulation onto titanium dioxide batch experiments, spectroscopy analysis and theoretical calculation, Sci. Rep. 7 (2017), https://doi.org/10.1038/srep39625 Article number: 39625.

[47] G. Williams, B. Seger, P.V. Kamt, $TiO_2$-graphene nanocomposites. UV-assisted photocatalytic reduction of graphene oxide, ACS Nano. 2 (2008) 1487–1491, https://doi.org/10.1021/nn800251f.

[48] T.D. Nguyen-Phan, V.H. Pham, E.W. Shin, H.D. Pham, S. Kim, J.S. Chung, E.J. Kim, S.H. Hur, The role of graphene oxide content on the adsorption-enhanced photocatalysis of titanium dioxide/graphene oxide composites, Chem. Eng. J. 170 (2011) 226–232, https://doi.org/10.1016/j.cej.2011.03.060.

[49] G. Hurwitz, G.R. Guillen, E.M.V. Hoek, Probing polyamide membrane surface charge, zeta potential, wettability, and hydrophilicity with contact angle measurements, J. Membr. Sci. 349 (2010) 349–357, https://doi.org/10.1016/j.memsci.2009.11.063.

[50] O. Coronell, B.J. Mariñas, D.G. Cahill, Depth heterogeneity of fully aromatic polyamide active layers in reverse osmosis and nanofiltration membranes, Environ. Sci. Technol. 45 (2011) 4513–4520, https://doi.org/10.1021/es200007h.

[51] V.T. Do, C.Y. Tang, M. Reinhard, J.O. Leckie, Degradation of polyamide nanofiltration and reverse osmosis membranes by hypochlorite, Environ. Sci. Technol. 46 (2012) 852–859, https://doi.org/10.1021/es203090y.

[52] C.Y. Tang, Y.N. Kwon, J.O. Leckie, Probing the nano- and micro-scales of reverse osmosis membranes-A comprehensive characterization of physiochemical properties of uncoated and coated membranes by XPS, TEM, ATR-FTIR, and streaming potential measurements, J. Membr. Sci. 287 (2007) 146–156, https://doi.org/10.1016/j.memsci.2006.10.038.

[53] F. Lufrano, V. Baglio, P. Staiti, A.S. Arico, V. Antonucci, Polymer electrolytes based on sulfonated polysulfone for direct methanol fuel cells, J. Power Sources 179 (2008) 34–41, https://doi.org/10.1016/j.jpowsour.2007.12.079.

[54] Y. Yampolskii, I. Pinnau, B.D. Freeman, Materials Science of Membranes for Gas and Vapor Separation, John Wiley & Sons Ltd, 2006 10.1002/047002903X.

[55] H. Lin, S.M. Thompson, A. Serbanescu-Martin, J.G. Wijmans, K.D. Amo, K.A. Lokhandwala, T.C. Merkel, Dehydration of natural gas using membranes. Part I: composite membranes, J. Membr. Sci. 413–414 (2012) 70–81, https://doi.org/10.1016/j.memsci.2012.04.009.

[56] R. Xing, Y. Rao, W. TeGrotenhuis, N. Canfield, F. Zheng, D.W. Winiarski, W. Liu, Advanced thin zeolite/metal flat sheet membrane for energy efficient air dehumidification and conditioning, Chem. Eng. Sci. 104 (2013) 596–609, https://doi.org/10.1016/j.ces.2013.08.061.

[57] A. Ito, Dehumidification of air by a hygroscopic liquid membrane supported on surface of a hydrophobic microporous membrane, J. Membr. Sci. 175 (2000) 35–42, https://doi.org/10.1016/S0376-7388(00)00404-X.

[58] P. Scovazzo, Testing and evaluation of room temperature ionic liquid (RTIL) membranes for gas dehumidification, J. Membr. Sci. 355 (2010) 7–17, https://doi.org/10.1016/j.memsci.2010.02.067.

[59] P.G. Ingole, M. Sohail, A.M. Abou-Elanwar, M. Irshad Baig, J.D. Jeon, W.K. Choi, H. Kim, H.K. Lee, Water vapor separation from flue gas using MOF incorporated thin film nanocomposite hollow fiber membranes, Chem. Eng. J. 334 (2018) 2450–2458, https://doi.org/10.1016/j.cej.2017.11.123.

[60] M.I. Baig, P.G. Ingole, W.K. Choi, S.R. Park, E.C. Kang, H.K. Lee, Water vapor permeation behavior of interfacially polymerized polyamide thin film on hollow fiber membrane substrate, J. Taiwan Inst. Chem. Eng. 60 (2016) 623–635, https://doi.org/10.1016/j.jtice.2015.11.010.

[61] P.G. Ingole, M.I. Baig, W. Choi, X. An, W.K. Choi, J.D. Jeon, H.K. Lee, Synthesis of superhydrophilic Nafion based nanocomposite hollow fiber membranes for water vapor separation, Chem. Eng. Res. Des. 127 (2017) 45–51, https://doi.org/10.1016/j.cherd.2017.09.003.

[62] P.G. Ingole, M.I. Baig, W. Choi, X. An, W.K. Choi, H.K. Lee, Role of functional nanoparticles to enhance the polymeric membrane performance for mixture gas

separation, J. Ind. Eng. Chem. 48 (2017) 5–15, https://doi.org/10.1016/j.jiec.2016.09.041.

[63] X. An, P.G. Ingole, W.K. Choi, H.K. Lee, S.U. Hong, J.D. Jeon, Development of thin film nanocomposite membranes incorporated with sulfated β-cyclodextrin for water vapor/N$_2$ mixture gas separation, J. Ind. Eng. Chem. 59 (2018) 259–265, https://doi.org/10.1016/j.jiec.2017.10.031.

[64] X. An, P.G. Ingole, W.K. Choi, H.K. Lee, S.U. Hong, J.D. Jeon, Enhancement of water vapor separation using ETS-4 incorporated thin film nanocomposite membranes prepared by interfacial polymerization, J. Membr. Sci. 531 (2017) 77–85, https://doi.org/10.1016/j.memsci.2017.02.045.

[65] A.M. Abou-Elanwar, Y.M. Shirke, P.G. Ingole, W.K. Choi, H. Lee, S.U. Hong, H.K. Lee, J.D. Jeon, Nanocomposite hollow fiber membranes with recyclable β-cyclodextrin encapsulated magnetite nanoparticles for water vapor separation, J. Mater. Chem. A 6 (2018) 24569–24579, https://doi.org/10.1039/C8TA09413F.